MEDICAL ROBOTS

Microrobotic laser steering for minimally invasive surgery

Peter A. York[1,2]*, Rut Peña[1,2], Daniel Kent[2,3], Robert J. Wood[1,2]

The creation of multiarticulated mechanisms for use with minimally invasive surgical tools is difficult because of fabrication, assembly, and actuation challenges on the millimeter scale of these devices. Nevertheless, such mechanisms are desirable for granting surgeons greater precision and dexterity to manipulate and visualize tissue at the surgical site. Here, we describe the construction of a complex optoelectromechanical device that can be integrated with existing surgical tools to control the position of a fiber-delivered laser. By using modular assembly and a laminate fabrication method, we are able to create a smaller and higher-bandwidth device than the current state of the art while achieving a range of motion similar to existing tools. The device we present is 6 millimeters in diameter and 16 millimeters in length and is capable of focusing and steering a fiber-delivered laser beam at high speed (1.2-kilohertz bandwidth) over a large range (over ±10 degrees in both of two axes) with excellent static repeatability (200 micrometers).

INTRODUCTION

In minimally invasive surgery, access is gained to internal anatomy through natural orifices or small external incisions. It encompasses diverse practices such as the catheter delivery of stents, flexible endoscopy of the gastrointestinal tract, laparoscopic treatment of abdominal diseases, and transnasal operation at the skull base for neurological conditions. Common to many of these procedures is the need for wristed articulation at the distal ends of tools for manipulating tissue and visualizing the surgical site (*1*). This was an important motivation for introducing robotics into minimally invasive surgery (*2*) and remains a vibrant area of research and development today (*3*–*5*).

This work addresses this large challenge by focusing on a subset of the tools used in minimally invasive surgery: those used for energy delivery. Common surgical energy sources include monopolar and bipolar radio frequency electric current (electrosurgery), thermal cautery (direct current heating), ultrasonic vibrations, argon beam coagulation (argon assists the conduction of radio frequency current), and lasers (*6*). These tools are essential to the surgical workflow because they enable the cutting, coagulation, and desiccation of tissue deep inside the body. The different energy sources ultimately have the same effect: denaturizing proteins through the heating of tissue. Moreover, they are, at present, used in a similar way, brought close (a few millimeters) to the tissue, and energy is delivered directly from the electrode or fiber to the anatomy.

However, a more sophistical approach is possible when it comes to delivering laser energy. Although current laser-based tools are used in the static, close-contact way (*7*–*10*), a robotic approach could be used to steer the laser. Because lasers can be focused and steered using low-inertia optical components, high-bandwidth distal actuation can be used to control the laser position. This would yield the same benefits that robotic wrists grant to mechanical end effectors (i.e., the ability to work around corners and navigate obstacles) while achieving additional capability to precisely control the speed of the laser on the tissue over a wide range. This is important because laser speed strongly affects the duration of laser irradiation, a critical determinant of the quality of laser-tissue interaction: incision depth, spread of thermal damage, and hemostatic effect (*11*–*13*).

The improved incision quality possible with robotic laser steering is demonstrated by Remacle *et al.* (*14*), who used an external laser manipulator to achieve delicate resections of vocal fold lesions. This system relies on a line-of-sight pathway through the airway, which limits its use in other surgical arenas. However, its capabilities provide a reasonable initial set of performance goals for an endoscopic laser steering system. It uses laser speeds of 29 mm/s and typical incision lengths of 0.5 to 3.5 mm (*15*). A range of motion larger than typical incision length is likely desirable for minimizing the repositioning needed of the fiber-delivery device. Similarly, increased laser speed is desirable for enabling operation with a wide variety of surgical lasers; appropriate laser speed increases with increased laser pulse frequency and laser spot size, assuming similar overlap between pulses is desired.

The challenge to creating this type of robotic device is the opto-electrical-mechanical complexity needed in a small package. Device diameter is the key constraint and depends on the type of surgical tool being used; a sampling of commonly used tools shows a range of different sizes: colonoscopes ranging from 9.7 to 14.8 mm (PCF-PH190I/L and CF-FH260AZI/L, Olympus Medical Systems), laparoscopic tools of either 5 or 8 mm (da Vinci SP, Intuitive Surgical), rhinolaryngoscopes for transnasal access ranging from 2.6 to 4.9 mm (ENF-V3 and ENF-VT3, Olympus Medical Systems), and cardiac catheters ranging from 2.67 to 3.33 mm, (AcuNav, Biosense Webster).

Several research groups have proposed solutions to the robotic laser steering problem, yielding two broad approaches, summarized in Table 1. In both, a flexible optical fiber delivers a laser to the end effector of a minimally invasive surgical tool. In the first approach, which we term "fiber steering," the tip of the fiber is robotically bent to control the spot position on the surgical site. This is the approach of Kundrat *et al.* (*16*, *17*), who embedded the laser fiber inside a two-segment continuum manipulator driven by push-pull rods. Similarly, Zhao *et al.* (*18*) used cables as mechanical transmissions to bend the distal tip of the optical fiber. The strength of these methods is their simplicity: They do not require complex manufacturing

[1]John A. Paulson School of Engineering and Applied Sciences, Harvard University, 150 Western Ave., Boston, MA, USA. [2]Wyss Institute for Biologically Inspired Engineering, 3 Blackfan Circle, Boston, MA, USA. [3]Beth Israel Deaconess Medical Center, 110 Francis St., Boston, MA, USA.
*Corresponding author. Email: pyork@g.harvard.edu

Table 1. Comparison to state of the art. Our microrobotic approach to laser steering allows miniaturization beyond what was previously achievable. We also achieve higher dynamic performance while maintaining a similar range of motion to existing devices. The device described in (*23*) was preliminary to the work described herein.

	Fiber steering			**Optical steering**			
	Kundrat	**Zhao**	**Acemoglu**	**Andreff**	**Patel**	**Bothner**	**This work**
	(*16*, *17*)	**(*18*)**	**(*19*)**	**(*20*, *21*)**	**(*22*)**	**(*23*)**	
Diameter (mm)	11.5	22	13	14	17	15	6
Length (mm)	45*	22	60	42	50	45	16
Working distance (mm)	20	1	30	20	25†	20	25
Range of motion (mm)	45 × 45	28 ⌀	4 × 4	20 × 20	26.5 ⌀	18 × 10	18 × 18
Maximum speed (mm/s)	3.5	3	94	33‡	167‡	2000	3900
Mechanical bandwidth (Hz)	–	–	63	270	–	750	1200

*Approximation based on published images. †Patel *et al.* tested their device at a long working distance (373 mm), which yielded a diametral range of motion of 396 mm. To facilitate comparison with the other state-of-the-art devices, we show their expected performance with a focal length suitable for the minimally invasive surgical application. ‡Calculated from published data.

of miniature actuators or sensors; moreover, they achieve large ranges of motion (45 mm by 45 mm and 28 mm in diameter, respectively). However, laser speed is limited (3 and 3.5 mm/s) by the use of cables and rods. Acemoglu *et al.* (*19*) struck a different balance. They used miniature electromagnetic coils to bend the fiber via a permanent magnet that is bonded to the fiber. They achieved a larger laser speed (94 mm/s), but because of pernicious trade-offs related to the size of the coils and permanent magnet, the range of motion was reduced to 4 mm by 4 mm—substantially less than the cable- and rod-driven devices.

In the second approach, called "optical steering," mirrors and/or prisms are used to control the laser spot position after it exits the flexible optical fiber. This approach was taken by Andreff *et al.* (*20*, *21*), who used linear piezoelectric motors to control the angle of a flexure-supported tip-tilt mirror. They achieved a moderate speed (33 mm/s) and range of motion (20 mm by 20 mm), but the optical configuration requires the use of an unwieldy external mirror that occludes the field of view and makes integration with focusing optics difficult. Patel *et al.* (*22*) provided a different approach in which they used miniature piezoelectric motors to rotate Risley prisms. They achieved a greater maximum speed (167 mm/s) with similar range of motion (26.5 mm in diameter). However, their use of rotary transmission elements makes further miniaturization challenging from the demonstrated diametral size of 17 mm.

We herein describe our advancements in design, fabrication, and control that allow us to surpass the performance of the state of the art in terms of miniaturization (6 mm in diameter) and laser speed (3900 mm/s) while achieving a similar range of motion (18 mm by 18 mm). Our approach, summarized in Movie 1, builds on our preliminary work Bothner *et al.* (*23*) in which we showed that piezoelectric bending actuators can be used in conjunction with miniature compliant mechanisms to generate the rotations of miniature mirrors in a compact package. In this work, we first lay out general design principles for building miniature laser galvanometers and develop the key insight that the use of three mirrors counterintuitively allows greater

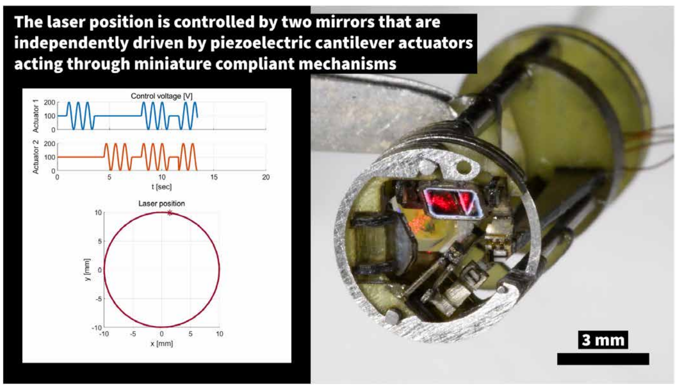

Movie 1. Overview of the microrobotic laser steering system.

miniaturization than two mirrors. This follows from ray tracing of the laser trajectory inside the galvanometer. Second, we use a modular fabrication technique in which individual components are placed on disks and assembled on a railed superstructure. This simplifies the typically challenging problem of assembling complex millimeter-scale systems and enables us to achieve a rich feature density. It also allows the device to be easily assembled and disassembled, which allows for rapid testing, debugging, and development. We also leverage printed-circuit micro-electro-mechanical systems techniques (PC-MEMS) for making miniature compliant mechanisms that allow us to generate large-angle mirror rotations without sacrificing miniaturization (*24*, *25*). Last, for control, we implement a low-dimensional hysteresis compensation scheme that corrects for the hysteresis in the piezoelectric bending actuators and intermediate mechanisms. In this work, we validate our microrobotic approach to laser steering using a low-powered visible laser, which facilitates testing and development, with the vision of integrating with surgical lasers in future work.

Of these contributions, the fabrication advancements will be most broadly useful within the robotics field. The problem of simple, repeatable device assembly is a bottleneck in the development of complex microrobotic devices, which we surmount using the disk-and-rail modular assembly technique. This method can be used and adapted for the construction of complex microrobotic devices, both within and outside of the medical robotics context. The design and control advancements are also important, but their impact will likely be more limited to the development of laser-based and/or piezoelectric-based microrobotic devices.

RESULTS

Our microrobotic laser steering device is 6 mm in diameter and can thus be seamlessly integrated into existing workflows in flexible gastroenterology and single-port surgery—settings in which adapting traditional tools is difficult and lasers are of particular interest (*26*). The laser steering tool is shown as a standalone device in Fig. 1A and integrated with a colonoscope (Olympus CF-100 L) in Fig. 1 (B and C). It is shown external to the colonoscope, but it is small enough to be internally integrated into a special-purpose flexible scope. The device is 16 mm in length and has the ability to steer a focused laser beam through over ±10° on two orthogonal axes with a 1.2-kHz mechanical bandwidth. Its principle of operation, demonstrated in movie S1, is as follows: A gradient-index collimating lens collects light from a ferrule-terminated optical fiber and directs it into a miniature plano-convex focusing lens. The light is reflected by a 45° angle-of-incidence mirror and into a miniature galvanometer. Flexible linkages convert the quasi-linear motion of piezoelectric bending actuators into the rotational motions of the galvanometer mirrors.

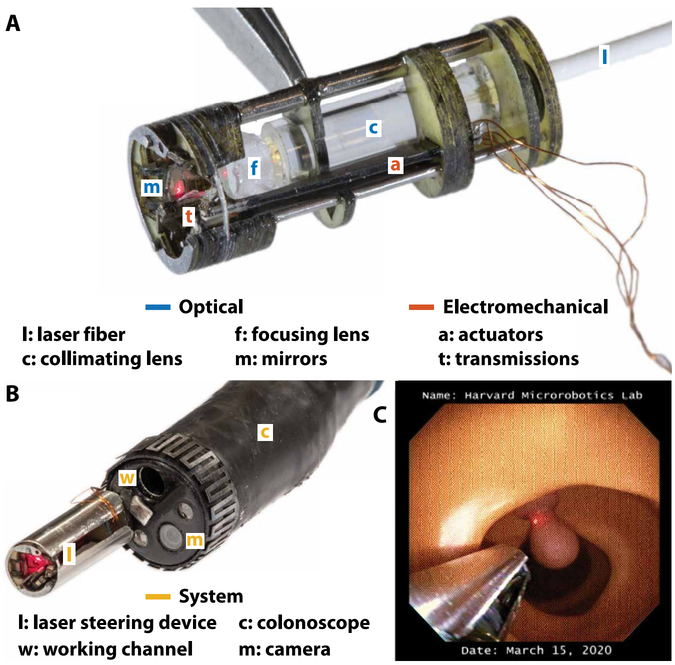

Fig. 1. Microrobotic laser steering device. (**A**) The 6-mm-diameter device receives a fiber-delivered laser, collects the light using a gradient-index collimator, focuses the light using a miniature plano-convex lens, and uses a miniature two-mirror galvanometer to control the angle of the exiting ray. (**B**) The laser steering device, partially encapsulated and affixed to a colonoscope. Because the device is sufficiently small, it can be integrated with the colonoscope while maintaining standard visualization, illumination, and working channel access. (**C**) The colonoscope view of a simulated polyp resection procedure. Note that the laser steering tool fills only a small portion of the visual field.

In this section, we describe the design, fabrication, and control insights that culminate in our laser steering solution. We first describe general design considerations for miniaturizing the galvanometer portion of the device. This is the least straightforward component to miniaturize both in terms of design and fabrication. Next, we present details for the design and construction of each component and the assembly thereof. Third, we report the methods used for static position control and characterization. Last, we describe the dynamic properties of the device, demonstrate the ability for high-bandwidth operation, and interface the device with a commercial colonoscope.

General design considerations

For the galvanometer design, the objective is to minimize the distance between the mirrors, given the beam size, mirror size, and desired range of motion, all while avoiding collisions between the mirrors and between the reflected beam and previous mirrors in the optical path (Fig. 2). An important high-level design consideration is the number of mirrors used. Somewhat counterintuitively, a three-mirror design can actually be made smaller than a two-mirror design, if the same range of motion is desired for each.

To see that this is the case, consider the three-mirror design shown in Fig. 2A: If the distance between the first and second mirrors is too small, then the reflected beam from the third mirror will intersect the first mirror. If the distance between the second and third mirrors is too small, then those mirrors will collide. However, increasing the distance between mirrors not only increases device size, but it also means that larger area mirrors are needed to collect the reflected light for the same range of motion. The three-mirror design shown balances all of these considerations to yield a device with ±10° range of motion on each active mirror in a 4-mm-diameter footprint. Note that the use of chamfered corners on the mirrors increases the range of motion by preventing collisions in critical locations.

The first two-mirror design (Fig. 2B) has the same diameteral footprint as the three-mirror design, but its range of motion is halved on the first-mirror axis. The loss in range of motion follows from an unfortunate set of trade-offs. If the mirrors are too close together, then the beam reflected from the second mirror will intersect the first mirror for large positive rotation angles of the first mirror. On the other hand, if the distance between the two mirrors is increased, then the second mirror must be enlarged to accept the incident light for large negative rotation angles of the first mirror. This is the second two-mirror design (Fig. 2C); it achieves the same range of motion as the three-mirror design (Fig. 2A) at the expense of a 50% increase in diameter.

Throughout this analysis, we assumed a collimated beam diameter of 1 mm. This is larger than the low-power pointing laser used herein for device validation, but it is a reasonable choice for a collimated high-power beam. For simplicity, we also chose the neutral position of each mirror to be at 45° angle of incidence with the incoming beam; allowing this to slightly deviate from 45° might yield slightly different results but would not change the structure of the design trade-offs. We also assumed that a symmetric range of motion is desired. Once again, if this was not the case, then the resulting design might change slightly, but the nature of the design space would not change. Last, it should be emphasized that we have been considering the case of the exiting ray being parallel to the incoming fiber [forward looking, per (*27*)]. If one wanted the exiting ray to be perpendicular

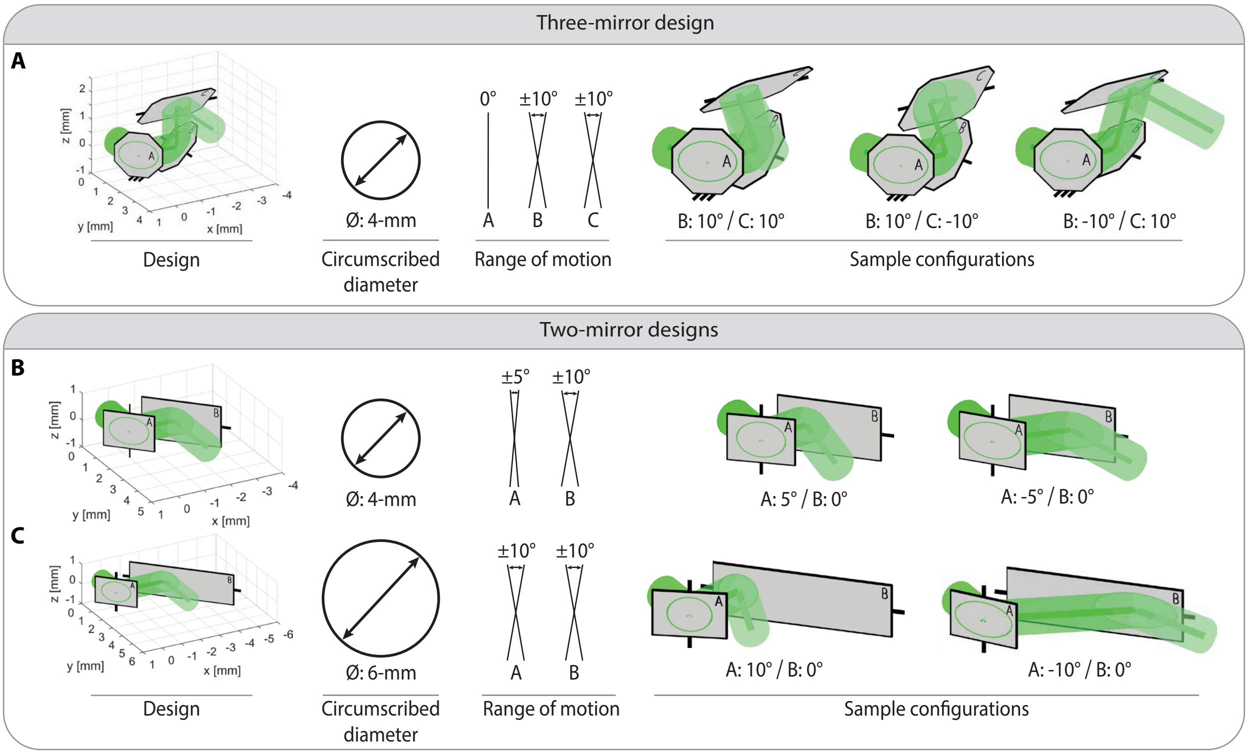

Fig. 2. Design for range of motion and miniaturization. (**A**) The three-mirror galvanometer achieves a larger range of motion than (**B**) a two-mirror design of the same size. (**C**) A two-mirror design with 50% larger diameter is needed to achieve the same range of motion as the three-mirror design. Range of motion is primarily determined by the ability of the mirrors to fully capture and reflect the incident light, but it is limited by the need to avoid collisions between mirrors and collisions between the reflected laser and previous mirrors in the optical path. Sample configurations show the limits of the range of motion.

to the incoming fiber (side looking), there would be no reason to use a three-mirror design; a two-mirror design would be perfectly acceptable in terms of miniaturization and range of motion. However, because most energy delivery tools used in surgery are forward looking, we chose to use that configuration for our device.

Another small point of differentiation between the three- and two-mirror designs for the forward-looking configuration is the shape of the focal plane. Because the distance that the laser travels through the three-mirror design changes very little as the mirror angles change, the focal plane is nearly symmetric about the neutral configuration. This is not the case for the two-mirror designs; the distance that the laser travels between the mirrors changes drastically with changing mirror angles. This yields the deformed focal plane that is contracted for large negative values of the first-mirror rotation angle, as seen in the previous version of this device (*23*).

Detailed design and fabrication

With those general insights in hand, we undertook the detailed design and fabrication of the device. For fabrication, we used a mixture of off-the-shelf components and custom-made parts that were primarily created using laser micromachining (Oxford Lasers E Series with Coherent Avia 355-7 laser). The assembled three-mirror galvanometer is shown in Fig. 3A, and each component before assembly is shown in Fig. 4. The assembly process is shown in full in movie S2. Specific details for component design, fabrication, and function are as follows:

1) Steel-rod superstructure. This component consists of two 500-μm- and one 300-μm- diameter stainless steel rods (Misumi USA) onto which the remaining components are assembled. The rods are orthogonally located into an FR4 disk using an alignment jig. A spring steel preload spring to compress and hold the assembled components in place is attached to the disk. All components were laser-micromachined.

2) Ferruled fiber and collimating lens. An off-the-shelf ferrule terminated optical fiber (SMP- F0106-FC, Thorlabs Inc.) was assembled with a gradient index collimator (GRIN2306A, Thorlabs Inc.) and attached to an FR4 support disk.

3) Piezoelectric bending actuators. These were made to size using the process and materials described in (*28*). We chose actuator dimensions in accordance with the available space adjacent to the optical components: active length of 7 mm, tip length of 1.8 mm, bridge length of 0.5 mm, base width of 1.4 mm, and tip width of 0.4 mm. The actuators are driven in the biased unipolar configuration with a fixed bias voltage, so each is controlled by a single time-varying input signal ranging from zero to the bias voltage. To achieve a sizeable output displacement while ensuring that the tensile strain in the piezoceramic is well below the failure limit, we chose a fixed bias voltage of 200 V. Under that drive condition, the actuators achieve free displacement of ±200 μm and have a first resonant frequency of 2.6 kHz.

4) Focusing lens. This was acquired as an off-the-shelf component (#89-003, Edmund Optics) and ground down to size using an alignment jig and a diamond cutoff wheel. Registration marks laser pre-engraved into the lens allow alignment of the optical center after grinding.

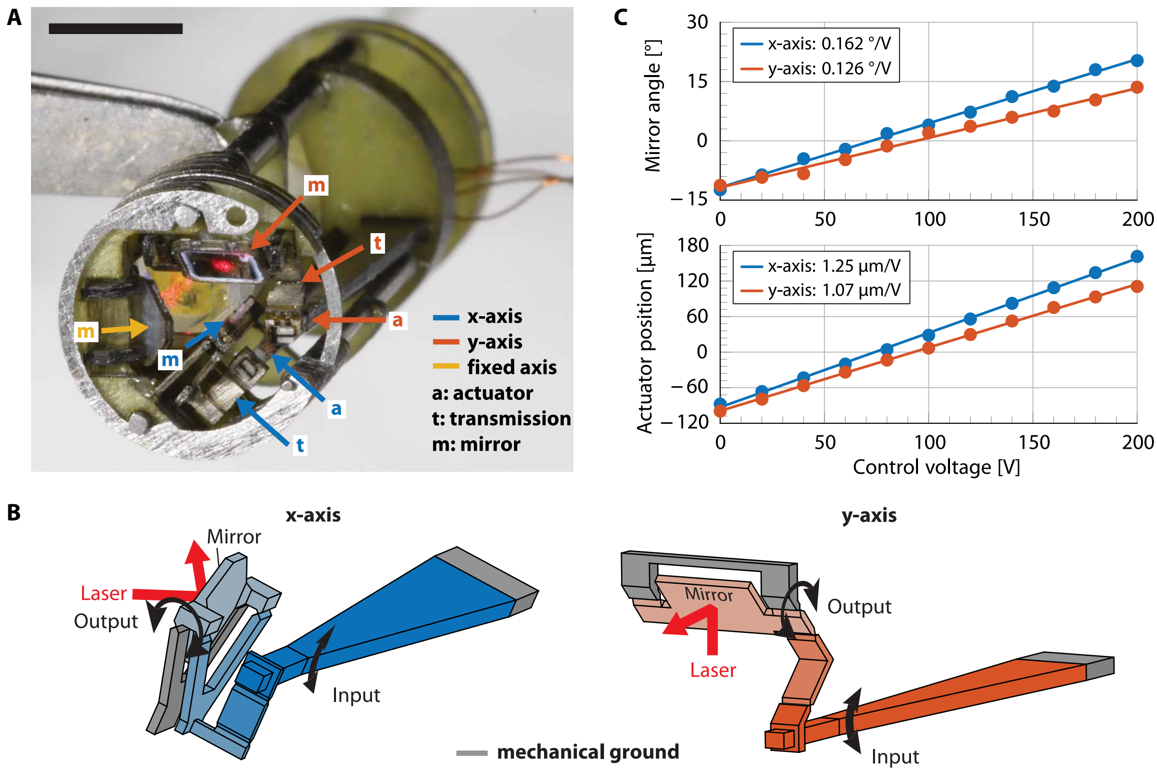

Fig. 3. Device components and kinematic structure. (**A**) Detailed view of the galvanometer. Piezoelectric bending actuators control the angles of the mirrors via compact motion transmissions made from compliant polyimide joints and rigid stainless steel links. Scale bar, 3 mm. (**B**) Kinematic structure of the two motion transmissions, which convert the quasi-linear (parabolic) input motion into rotational motion of the mirrors. They are shown in roughly the same orientation as in the above image. (**C**) Measured linkage kinematics showing the nominal relationships between control voltage, actuator position, and mirror angle. These relationships are not used directly for control; rather, they validate the designed linkage stiffnesses and transmission ratios.

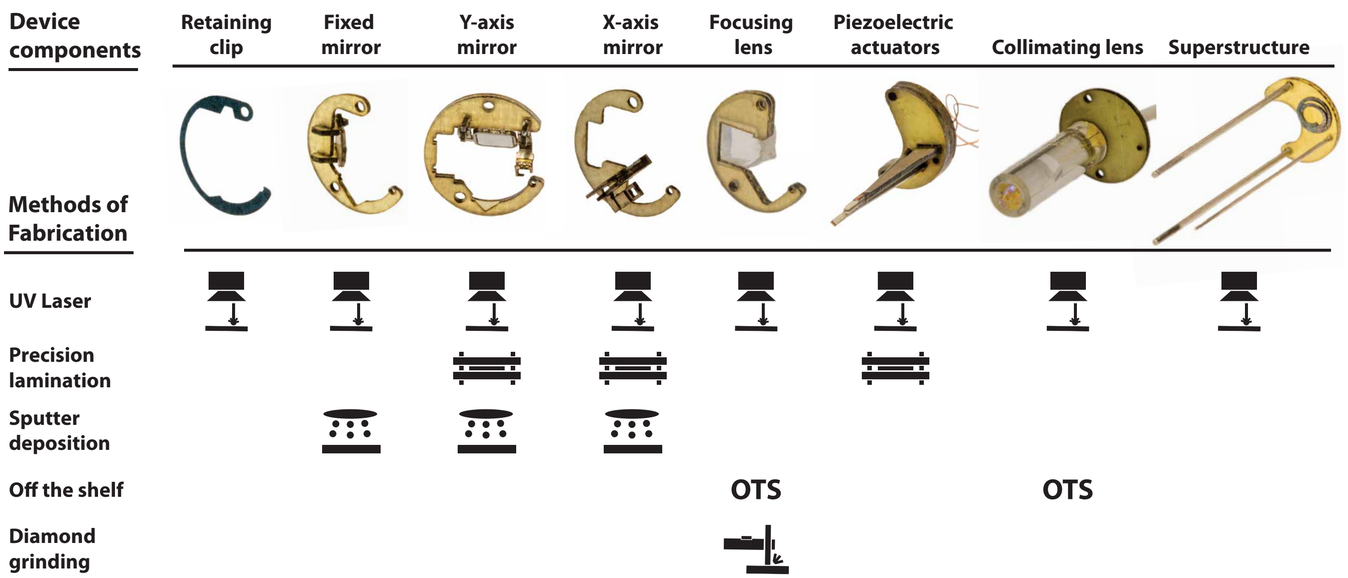

Fig. 4. Device components and fabrication. The key components of the laser steering device are shown in assembly order from the superstructure to the retaining clip. The icons below each component show the methods of fabrication used.

5) Articulable mirrors and motion transmissions. These are complex assemblies of rigid and flexible components fabricated using PC-MEMS. They consist of crank-slider linkages formed from stainless steel, polyimide, and a heat-curable acrylic adhesive (Pyralux FR1500, Dupont Inc.). The mirrors are located on the cranks, and the sliders each interface with one of the piezoceramic actuators, as

shown schematically in Fig. 3B. The x-axis transmission additionally contains a linearizing linkage to compensate for the out-of-plane motion of the bending actuator tip. The mirrors are made from sputtered aluminum (Denton Desktop Pro, Denton Vacuum LLC) on a 100-μm fused silica substrate and singulated using an ultraviolet laser.

The detailed design of the transmissions follows from the actuator properties. We wanted to achieve at least ±10° of motion for each mirror, in accordance with the state of the art. To achieve this in our device, there are two important design considerations: (i) the transmission ratio of each linkage and (ii) the stiffness of each linkage relative to that of the actuators. On the basis of experience sizing similar mechanical components (*29*), we chose a target transmission ratio of 0.1°/μm and a target stiffness equal to that of the actuators. In the device, we achieved transmission ratios of 0.13° and 0.12°/μm (due to small fabrication errors) and stiffnesses of 60 and 90% the actuator stiffness, respectively, as can be seen in the experimental data (Fig. 3C). Note that the stiffness of the transmission is in parallel to the actuator stiffness and results in reduction of the free displacement of the actuators. Thus fabricated, we achieve ranges of motion −12.5° to 20° and −11.2° to 13.7° for the two mirrors, respectively. The asymmetry corresponds to small assembly misalignment and slightly nonlinear transmission kinematics. The neutral (zero) mirror angles and actuator positions correspond to the configuration for which the output beam is aligned along the longitudinal axis of the device.

6) Fixed mirror. This aluminum-sputtered fused silica mirror is fixed at 45° relative to the incident light using two alignment blocks that in turn interface with an FR4 support disk.

7) Retaining clip. This spring steel component fits onto grooves rastered into the stainless steel rods of the superstructure. It axially constrains the assembly in conjunction with the preload spring located on the superstructure base.

8) Spacer tubes and disks. These pieces are laser micromachined to ensure proper spacing and alignment between components. Tube length and disk thickness are the critical dimensions.

Position control and characterization

We began characterizing the device by measuring open-loop repeatability, which is an important metric because it describes the fundamental limitations of the device physics to reproduce identical motions. Stiction, plasticity, and other phenomenon mean that identical inputs do not produce identical outputs. Unidirectional repeatability is a measure of repeatability in which measurement points are only approached from one direction. Measurement results for unidirectional repeatability are shown in Fig. 5A. The maximum 2σ standard distance of the sampled points is 200 μm, which means that there is 95% confidence that any series of identical movements will fall within a 200-μm radius of dispersion about the mean trajectory.

The presence of hysteresis complicates position control. Hysteresis is a bidirectional effect that arises primarily from domain reorientation inside the piezoceramic actuator; it means that the laser position depends on the time history of the input. This is clearly undesirable because it complicates control and makes use of the device unintuitive. To minimize the hysteretic effects, we implemented a feed-forward compensation scheme, which is described in detail in Materials and Methods. To validate our approach, we commanded the star trajectories shown in Fig. 5 (B and C) and movie S3 for uncompensated and compensated inputs. The raw inputs clearly show the effects of path dependence, whereas the corrected inputs show improved tracking; this is, essentially, a measure of bidirectional repeatability. Quantitatively, we find that the maximum 2σ standard distance around the set points is 2.14 mm without compensation and 0.72 mm with compensation. This is reasonable improvement for feed-forward compensation; further improvement can be achieved with feedback control.

Because of the low dimensionality of the workspace and input space and the lack of sensor information, we chose to control the device using a direct model-free mapping between actuator input and laser spot position, cascaded with the feed-forward compensation for hysteresis. We fit third- and second-degree polynomial surfaces to the open-loop repeatability measurement data for the first and second mirrors, respectively. These fits were centered around 73 and 93 V for the x- and y-axis actuators, respectively, which correspond to neutral angles of the mirrors. The size of the "calibrated workspace" formed in this way was 18 mm by 18 mm, which is slightly smaller than the about 22 mm by 22 mm uncalibrated workspace shown in Fig. 5A.

Dynamic control and characterization

The bandwidth of the system is limited by resonant oscillation of the mirrors at high frequencies. The primary resonant frequencies for the two mirrors are 1.8 and 1.9 kHz, as can be seen in the Bode plots shown in Fig. 6 (A and B). In addition, there is a lower-frequency mode at 1.2 kHz on the first mirror (likely due to twisting or another off-axis mode). To avoid exciting these modes, we use a finite jerk motion profiling scheme (also known as sigmoid or S profiling) as seen in movie S4. The time histories of those trajectories are shown in fig. S4.

The system shows only minor deviation from static trajectories at high speeds, as can be seen in Fig. 6 (C and D) and movie S5. There is only 5% deviation between the trajectories followed at low (7.8 mm/s) and high (3900 mm/s) speeds. Also, because of the two-axis control, the system can trace complex planar trajectories, as shown in Fig. 6 (E and F) and movie S6. The large bandwidth in the system can also be exploited to generate multimodal profiles, as seen in movie S7. These are trajectories in which a high-frequency input is superimposed onto a low-frequency one. This allows the user to change the effective laser spot size on the fly, which is particularly relevant for situations in which a large area needs to be controllably covered, as in large-area hemostasis.

Colonoscope interfacing

Because of the low profile and small mass of the laser steering device (717 mg), it can be readily interfaced with existing surgical tools. To demonstrate this, we attached it onto the end of a colonoscope (Olympus CF-100 L) and performed a simulated polyp resection task on a benchtop surgical simulator, which can be seen in Fig. 1C and movie S8. We demonstrate both teleoperated control using a standard input device (Phantom Omni, Sensable Technologies) and robotic high-speed control of the laser along a registered incision trajectory. The system architecture and mapping used for teleoperation are described in Materials and Methods.

DISCUSSION

In this work, we describe microrobotic advances that point the way forward to new methods of controlling lasers in minimally invasive surgery. Ultimately, we anticipate that giving surgeons greater control

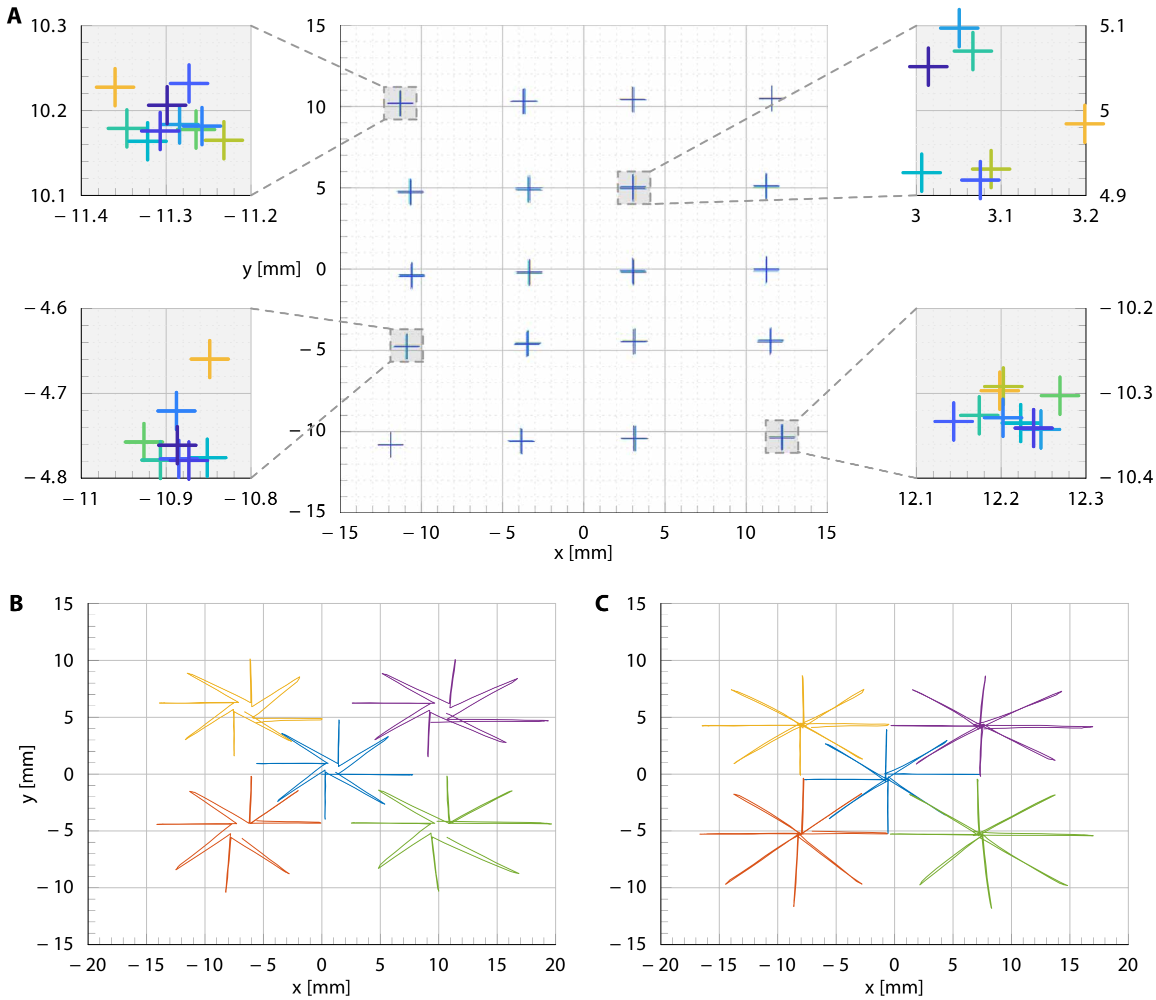

Fig. 5. Laser position control. (**A**) Laser position repeatability measurements with details shown in zoomed-in plots. (**B**) Set-point regulation without hysteresis compensation and (**C**) with compensation for the hysteresis arising from domain reorientation within the piezoelectric actuators. Colors represent individual trials.

over laser speed when interacting with tissue will enable the quality of laser-tissue interactions to be more widely tuned and optimized than possible with existing statically wielded tools. We also expect that robotic steering of lasers will improve access to areas difficult to reach with rigid tools. Last, we envisage that the use of steerable, focused lasers will allow energy to be delivered to tissue without occluding the surgeon's field of view. These are the ultimate aims toward which this work represents an important milestone.

Several technical challenges remain, primary of which is the incorporation of high-powered surgical lasers and suitable optical components. The choice of optical materials depends on the wavelength and power of the laser being used. For example, if a CO_2 laser is being used, gold-sputtered aluminum mirrors and zinc selenide lenses provide appropriate reflectance and transmission, respectively. Particular attention must be paid to the "laser-induced damage threshold," which is a measure of the laser power that an optical component can experience before degradation. Details for the scaling of the optical components when used with a particular surgical laser are given in the Supplementary Materials.

Regardless of the laser modality used, the device will need to be encapsulated so as to be robust to the fluids and debris in the surgical environment and allow for sterilization. Cleaning and safety protocols will need to be developed. Because the tips of laser fibers can be damaged after extended use, it may be advantageous to incorporate a method for decoupling the laser fiber from the device. This would allow the independent cleaning and cleaving of the laser fiber, which can expand its lifetime (*30*).

Conversely, it may be desirable to directly embed the device into a flexible endoscope. This would simplify the encapsulation and robustness challenges and prevent the device from partially occluding the scope's field of view. The downside of this approach would likely be an increase in cost because a dedicated endoscope would be needed instead of an add-on to existing endoscopes. Kiesslich *et al.* (*31*) demonstrated this integrated approach with a similar device by embedding a 5-mm-diameter, 43-mm-long confocal microscope into a standard flexible colonoscope. Our device is slightly larger in diameter and shorter in length than theirs, but it is similar enough in size to be similarly deployed.

The lack of intrinsic tactile feedback is a limitation of noncontact energy delivery methods, including the laser-based approach described here. To remedy this, several researchers have proposed haptic feedback schemes. Rizun *et al.* (*32*) described the basic concept of generating

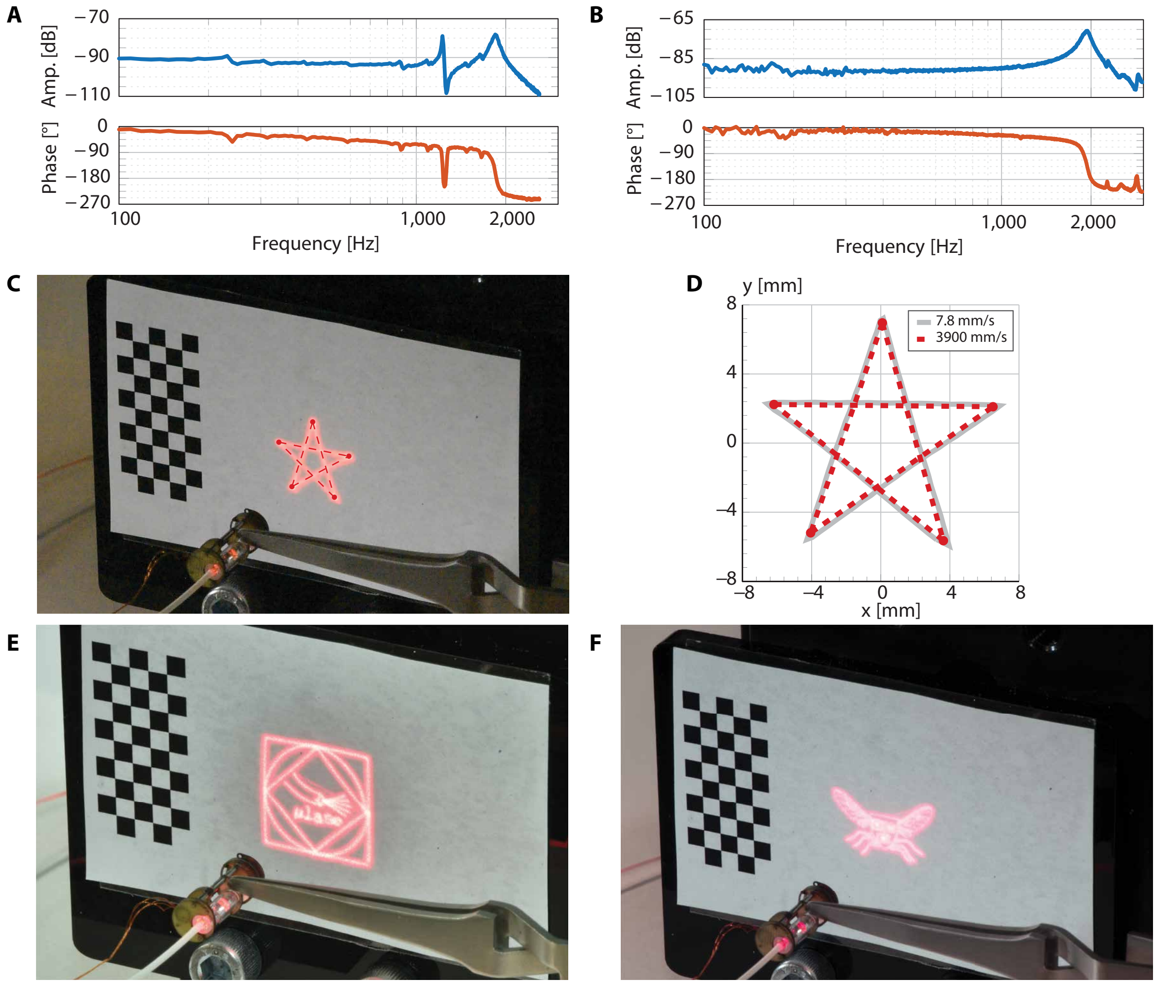

Fig. 6. High-speed control. (**A**) First-mirror (*x*-axis) frequency response to low-voltage white-noise input. (**B**) Second-mirror (*y*-axis) frequency response. (**C**) An image created by high-speed motion of the laser steering system. (**D**) The high-speed image closely matches the trajectory followed by the laser system at low speeds. There is only 5% deviation between the two trajectories, despite a difference in speed of 500×. (**E** and **F**) Complex images captured through long-exposure photography that demonstrate the system's intricate control capabilities.

a virtual surface corresponding to the surgical site and modulating the laser power based on the user's interactions with the virtual surface. In a more sophisticated scheme, Fichera *et al.* (*33*) used an estimation of laser incision depth to generate haptic interaction for the user. Other researchers, including Olivieri *et al.* (*34*) and Kundrat *et al.* (*16*), have investigated generating active constraints along desired trajectories to help guide the user's movement. There seems to be merit to each of these schemes, with the correct approach for a given task being application dependent. In laryngeal applications, in which retention of healthy tissue is critical, this might involve using active constraints to guide incisions away from healthy tissue, whereas in gastrointestinal applications, for which perforation of the bowels is a major complication, a haptic feedback scheme incorporating incision depth information may be preferable. This remains an important area for systematic exploration and technology development for laser-based surgical tools.

To achieve accuracy in line with the repeatability of the device, sensory feedback will need to be incorporated. A simple approach would be to embed strain gauge sensors within the piezoelectric bending actuators (*35*) to estimate actuator position and to use current sensing to estimate actuator velocity (*36*). The mirror position could then be calculated from the transmission kinematics and the laser position estimated from the model of specular reflection described in our prior work (*23*). Measuring the mirror position directly would result in a better laser position estimate, but the pathway to a suitable miniature sensing method is not as straightforward as sensing the actuator motion. Alternatively, visual feedback could be used for high-quality estimates, albeit with lower sample rates than achievable with electromechanical sensors. In practice, a sensor fusion that blends these different pieces of information is likely the best approach.

Our laser steering approach also may enable new approaches for endoscopic visualization and visual biopsy. In optical coherence tomography and confocal endomicroscopy, laser-tissue interactions are used to visualize subsurface structures, and scanning allows a large area of tissue to be seen at once. Optical steering can also be used to increase the effective field of view of standard white-light imaging tools, through stitching together a set of images acquired through rapid scanning. The scanning system and modular device assembly approach that we describe can be adapted to the fabrication of millimeter-sized versions of those systems. Even smaller versions of these systems

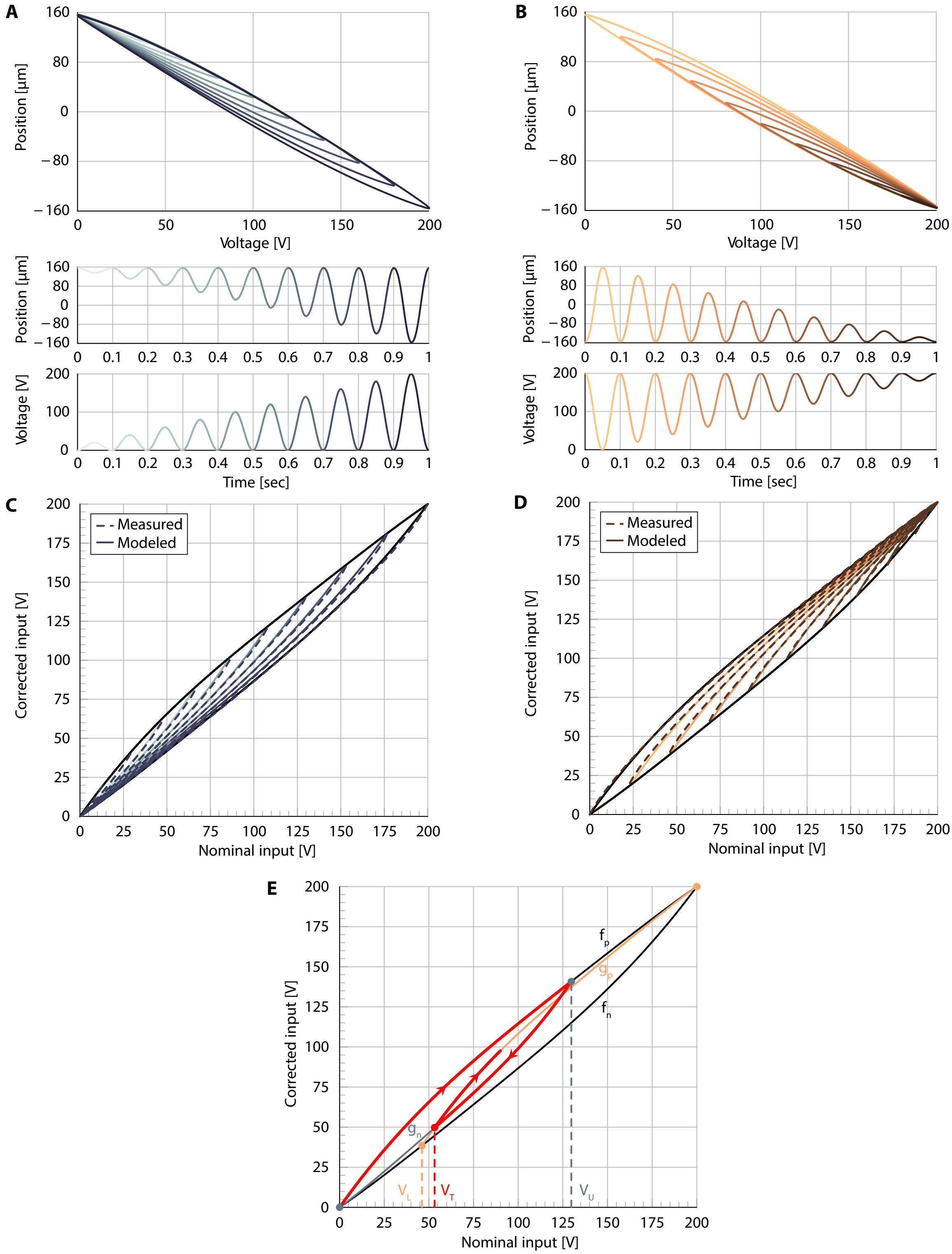

Fig. 7. Hysteresis measurement and modeling. (**A** and **B**) Amplitude-rich voltage inputs yield the hysteresis curves that are shown. These curves are scaled and inverted to yield the curves shown in (**C** and **D**), which are plotted together with the fitted model behavior. (**E**) Hysteresis model with key functions and parameters shown. The outer envelope is defined by the curves f_p and f_n, and the inner family of curves are defined by g_p and g_n. The subscript denotes the sign of the input rate (positive or negative). The sample trajectory shown in red shows the process of calculating the corrected input for a given nominal input.

are built using MEMS techniques (*27*) that use electrostatic and electrothermal actuators to excite resonant scanning elements. Our approach does not supplant these MEMS devices when absolute miniaturization is desired, but it does present advantages in terms of simplicity of construction and the ability to achieve a large quasi-static range of motion.

We also anticipate that this technology can be adapted for use in other microrobotic systems, particularly in micro aerial vehicles and satellites for which size and weight are at a premium (*29*, *37*). This technology will enable the fabrication of miniature light detection and ranging sensors used for mapping and navigation (*38*), as well as laser scanners used for wide-area atmospheric sensing of pollution (*39*).

MATERIALS AND METHODS

Hysteresis modeling and compensation

Because of hysteresis, actuator position is not a simple function of input voltage; rather, it depends on input voltage, input voltage history, and the current sign of the input. This complicates the position control problem, but by modeling and understanding this relationship, we can largely remove the hysteretic effects through inverting the hysteresis model and using it as a feed-forward control term. We began by capturing displacement response data for an unloaded bimorph actuator for two amplitude-rich input conditions, shown in Fig. 7 (A and B). This is a standard approach for capturing the effects of hysteresis throughout the input space. We then mapped the displacement data to the same range as the input space and inverted the relationship, yielding the curves shown in shown in Fig. 7 (C and D). These are the curves to parameterize and use in feed-forward control.

We undertake this parameterization using a modified version of the polynomial basis function approach described in (*40*). Our approach is to use two families of quadratic weighted sine functions, one for the positive-going curves and one for the negative-going curves. Implementation is as follows, using Fig. 7E as a visual guide. The outer curves f_p and f_n that form the hysteretic envelope are defined as

$$f_p(V) = V_{max}\left(a_p(V-h_p)^2 + k_p\right)\sin(\pi V/2V_{max})$$

$$f_n(V) = V_{max} + V_{max}\left(a_n(V-h_n)^2 + k_n\right)\sin(\pi(V-V_{max})/2V_{max})$$

where V_{max} is the maximum excursion of the input voltage. With these expressions, we first need to ensure that f_p and f_n are equal at the minimum and maximum excursions of the input voltage. We already have that $f_p(0) = 0$ and $f_n(V_{max}) = V_{max}$, but we also want to ensure that $f_p(V_{max}) = V_{max}$ and $f_n(0) = 0$. This leads to the choices of

$$a_p = \frac{1-k_p}{(V_{max}-h_p)^2} \quad a_n = \frac{1-k_n}{h_n^2}$$

Note that k_p and k_n control the size of the hysteresis loops and h_p and h_n control the shape. In anticipation of scaling these curves to the interior of the hysteretic envelope, we rescale h_p and h_n using the relations

$$h_p = l_p V_{max} \quad h_n = l_n V_{max}$$

Thus, the parameters k_p, k_n, l_p, and l_n fully define the shape of f_p and f_n, for a chosen value of V_{max}.

Now, the positive-going family of curves g_p and negative-going family of curves g_n can be defined as follows:

$$g_p(V, V_L) = f_n(V_L) + V_{amp}\left(a_p(V-h_p)^2 + k_p\right)\sin(\pi(V-V_L)/T)$$

$$g_n(V, V_U) = f_p(V_U) + V_{amp}(a_n(V-h_n)^2 + k_n)\sin(\pi(V-V_U)/T)$$

where V_L and V_U parameterize the curve families and V remains the independent variable. As seen in Fig. 7E, V_L denotes the point at which g_p intersects f_n, and V_U denotes the point at which g_n intersects f_p. Now, to make sure that each family of curves scales appropriately in size and shape, we have the constraints for the g_p family of curves:

$$V_{amp} = V_{max} - f_n(V_L) \quad T = 2(V_{max} - V_L)$$

$$h_p = l_p V_{max} + (1-l_p)V_L \quad a_p = \frac{(1-k_p)}{(V_{max}-h_p)^2}$$

Similarly, for the g_n family of curves we choose

$$V_{amp} = f_p(V_U) \quad T = 2V_U$$

$$h_n = l_n V_U \quad a_n = \frac{(1-k_n)}{h_n^2}$$

With these constraints, the parameters k_p, k_n, l_p, and l_n fully define g_p and g_n for some value of V_{max}.

The curves g_p and g_n are then used to calculate the corrected input from some nominal input. The current value of V_L or V_U denotes which member of g_p or g_n the system is operating on, and when the sign changes, the first step is to look for a new V_L or V_U. The transition point at which this occurs is denoted V_T, and to determine which new curve to transition onto, one solves the nonlinear root-finding problem:

$$g_p(V_T, V_L) - g_n(V_T, V_U) = 0$$

for the unknown variable (either V_L or V_U). With this in hand, one can calculate the desired feed-forward correction factor (g_p or g_n) for the current nominal input voltage. The process of finding the corrected input for a given nominal input is shown for a sample trajectory in Fig. 7E.

Using this approach, the measured curves are fit to the parameters ($k_p = 0.81$, $l_p = 0.5$, $k_n = 0.80$, and $l_n = 0.53$), as shown in Fig. 7 (C and D). In practice, the loading from the hinged transmissions slightly deforms these curves; for in situ hysteresis compensation, we used a tuned set of parameters ($k_p = 0.82$, $l_p = 0.5$, $k_n = 0.75$, and $l_n = 0.608$). Last, note that this is a quasi-static approach; piezoelectric hysteresis has some rate dependence, but we found the simple rate-independent approach to be sufficient for this application and the range of frequencies used.

Experimental setup and procedures

Laser position measurements

Laser position data were collected using a calibrated high-speed camera (Phantom v710, Vision Research Inc., Wayne, NJ) at 1200 pixel–by–800 pixel resolution with a macro lens (Nikon AF Micro-Nikkor 200 mm f/4D IF-ED). The camera has a maximum frame rate of 7500 frames/s at full resolution. Lighting was provided by two low-flicker light-emitting diode lights (Zaila, Nila Inc., Altadena, CA). This measurement setup is shown in fig. S2A. Reprojection errors from the calibration were less than 0.2 pixel (10 μm at the chosen focal length). Subpixel reprojection error means that the camera calibration captures the physics of the measurement setup well and that camera calibration is an only minor source of measurement error. Larger contributors are likely to be differences in lighting and marker detection. The measurement resolution in the camera orientation used for data collection was 46 and 51 μm per pixel in the world x and y directions, respectively.

Teleoperation architecture

A teleoperation system maps the user's control of a joystick input device (Phantom Omni, Sensable Technologies) onto the motion of the laser. We use a clutching scheme in which the system only registers the user's input if a button on the joystick is pressed. This allows the user to reposition their body on the fly to maintain a dexterous grasp of the input device. The pose of the input device is collected using the OpenHaptics Toolkit (3D Systems, Rock Hill, SC). During each software loop, the body frame difference (T_d) between current (T_c) and previous (T_p) input device poses is calculated according to

$$T_\mathrm{d} = T_\mathrm{p}^{-1} T_\mathrm{c}$$

where T_d, T_p, and T_c are members of SE(3). The x and y components of the body linear velocity (v_x and v_y) are then given by

$$v_x = T_{\mathrm{d},14}/\Delta t$$

$$v_y = T_{\mathrm{d},24}/\Delta t$$

where Δt is the loop time. These components are used because they point orthogonal to the joystick body and thus provide a natural basis for the laser control. This desired laser velocity is sent to a computer running a real-time operating system (xPC Target, MathWorks, Natick, MA) that scales the desired velocity and integrates to generate a desired position, which is then mapped to control voltages using the calibration and feed-forward mapping. Last, the control voltages are amplified using a piezoelectric amplifier (Trek PZD 350A, Advanced Energy Industries Inc., Denver, CO). The system architecture is illustrated graphically in fig. S2 (B and C).

Kinematics

We measured the relationship between actuator displacement and mirror angle for the entire input space in 20-V increments using a high-zoom inspection camera (Pixel-link PL- B741F). The resolution of the measurement system was 2.5 μm per pixel.

Repeatability

We undertook unidirectional repeatability measurements using the standard for single-axis motion control systems [International Organization for Standardization (ISO) 230-2]. Under these guidelines, we measured 20 different points in the laser workspace 10 times each, for a total of 200 data points. For each measurement, the system was powered off and reset, so as to eliminate the influence of hysteretic effects. A typical dataset of 20 points is shown in fig. S3; this image contains all 20 sampled points superimposed onto a single image.

Bandwidth and actuator performance

The frequency responses of the unloaded actuators and the full actuator/transmission/mirror subsystems were measured using a laser Doppler vibrometer (PSV-500, Polytec GmbH, Waldbronn, Germany). The static displacement and hysteresis characteristics of the bare actuators were measured using the same system.

SUPPLEMENTARY MATERIALS

robotics.sciencemag.org/cgi/content/full/6/50/eabd5476/DC1

Supplementary Text

Fig. S1. Time history of step and sigmoid responses.

Fig. S2. Experimental setup and system architecture.

Fig. S3. Measurement of laser position repeatability.

Fig. S4. Optical component schematic.

Movie S1. Principle of operation.

Movie S2. Device assembly.

Movie S3. Hysteresis compensation.

Movie S4. Sigmoid profiling of control inputs.

Movie S5. High-speed trajectory following.

Movie S6. Complex trajectory following.

Movie S7. Multimodal control.

Movie S8. Colonoscope integration and deployment.

REFERENCES AND NOTES

1. R. H. Taylor, A perspective on medical robotics. *Proc. IEEE* **94**, 1652–1664 (2006).
2. J. H. Palep, Robotic assisted minimally invasive surgery. *J. Minim. Access Surg.* **5**, 1–7 (2009).
3. P. J. Swaney, P. A. York, H. B. Gilbert, J. Burgner-Kahrs, R. J. Webster III, Design, fabrication, and testing of a needle-sized wrist for surgical instruments. *J. Med. Devices* **11**, 0145011–0145019 (2017).
4. J. Kim, W. Lee, S. Kang, K.-J. Cho, C. Kim, A needlescopic wrist mechanism with articulated motion and kinematic tractability for micro laparoscopic surgery. *IEEE/ASME Trans. Mechatron.* **25**, 229–238 (2020).
5. K. Chandrasekaran, A. Thondiyath, Design of a tether-driven minimally invasive robotic surgical tool with decoupled degree-of-freedom wrist. *Int. J. Med. Robot.* **16**, e2084 (2020).
6. G. Sankaranarayanan, R. R. Resapu, D. B. Jones, S. Schwaitzberg, S. De, Common uses and cited complications of energy in surgery. *Surg. Endosc.* **27**, 3056–3072 (2013).
7. P. Kronenberg, O. Traxer, Update on lasers in urology 2014: Current assessment on holmium:yttrium–aluminum–garnet (Ho:Yag) laser lithotripter settings and laser fibers. *World J. Urol.* **33**, 463–469 (2015).
8. G. E. Tontini, H. Neumann, A. Rimondi, S. Vavassori, B. Bruni, G. Cattignoli, P.-H. Zhou, L. Pastorelli, M. Vecchi, Ex vivo experimental study on the thulium laser system: New horizons for interventional endoscopy (with videos). *Endosc. Int. Open* **5**, E410–E415 (2017).
9. M. Karaman, T. Gün, B. Temelkuran, E. Aynacı, C. Kaya, A. M. Tekin, Comparison of fiber delivered CO_2 laser and electrocautery in transoral robot assisted tongue base surgery. *Eur. Arch. Otorhinolaryngol.* **274**, 2273–2279 (2017).
10. V. S. Vanni, J. Ottolina, G. Candotti, L. M. Castellano, I. Tandoi, F. D. E. Stefano, G. Poppi, S. Ferrari, M. Candiani, Flexible CO_2 laser fiber: First look at the learning curve required in gynecological laparoscopy training. *Minerva Ginecol.* **70**, 53–57 (2018).
11. A. S. Schimberg, T. M. Klabbers, D. J. Wellenstein, F. Heutink, J. Honings, I. van Engen-Van Grunsven, R. M. Verdaasdonk, R. P. Takes, G. B. van den Broek, Optimizing settings for office-based endoscopic CO_2 laser surgery using an experimental vocal cord model. *Laryngoscope* **130**, E680–E685 (2020).
12. M. A. Ansari, M. Erfanzadeh, E. Mohajerani, Mechanisms of laser-tissue interaction: II. Tissue thermal properties. *J. Lasers Med. Sci.* **4**, 99–106 (2013).
13. A. J. Welch, M. J. C. Van Gemert, *Optical-thermal Response of Laser-irradiated Tissue* (Springer, 2011), vol. 2.
14. M. Remacle, G. Lawson, M.-C. Nollevaux, M. Delos, Current state of scanning micromanipulator applications with the carbon dioxide laser. *Ann. Otol. Rhinol. Laryngol.* **117**, 239–244 (2008).
15. L. Reinisch, C. G. Garrett, Laryngeal temperature simulations during carbon dioxide laser irradiation delivered by a scanning micromanipulator. *Lasers Med. Sci.* **34**, 1011–1017 (2019).
16. D. Kundrat, A. Schoob, T. Piskon, R. Grässlin, P. J. Schuler, T. K. Hoffmann, L. A. Kahrs, T. Ortmaier, Toward assistive technologies for focus adjustment in teleoperated robotic non-contact laser surgery. *IEEE Trans. Med. Robot. Bionics* **1**, 145–157 (2019).
17. D. Kundrat, R. Graesslin, A. Schoob, D. T. Friedrich, M. O. Scheithauer, T. K. Hoffmann, T. Ortmaier, L. A. Kahrs, P. J. Schuler, Preclinical performance evaluation of a robotic endoscope for non-contact laser surgery. *Ann. Biomed. Eng.* 10.1007/s10439-020-02577-y, (2020).
18. M. Zhao, T. J. C. O. Vrielink, A. A. Kogkas, M. S. Runciman, D. S. Elson, G. P. Mylonas, LaryngoTORS: A novel cable-driven parallel robotic system for transoral laser phonosurgery. *IEEE Robot. Autom. Lett.* **5**, 1516–1523 (2020).

19. A. Acemoglu, D. Pucci, L. S. Mattos, Design and control of a magnetic laser scanner for endoscopic microsurgeries. *IEEE/ASME Trans. Mechatron.* **24**, 527–537 (2019).
20. K. Rabenorosoa, B. Tasca, A. Zerbib, P. Rougeot, N. Andreff, T. E. Pengwang, Squipabot: A mesoscale parallel robot for a laser phonosurgery. *Int. J. Optomechatron.* **9**, 310–324 (2015).
21. R. Renevier, B. Tamadazte, K. Rabenorosoa, L. Tavernier, N. Andreff, Endoscopic laser surgery: Design, modeling, and control. *IEEE/ASME Trans. Mechatron.* **22**, 99–106 (2017).
22. S. Patel, M. Rajadhyaksha, S. Kirov, Y. Li, R. Toledo-Crow, Endoscopic laser scalpel for head and neck cancer surgery. *Proc. SPIE* **8207**, 82071S (2012).
23. S. A. Bothner, P. A. York, P. C. Song, R. J. Wood, A compact laser-steering end-effector for transoral robotic surgery, in *IEEE International Conference on Intelligent Robots and Systems* (IEEE, 2019), pp. 7091–7096.
24. J. P. Whitney, P. S. Sreetharan, K. Y. Ma, R. J. Wood, Pop-up book MEMS. *J. Micromech. Microeng.* **21**, 115021 (2011).
25. P. S. Sreetharan, J. P. Whitney, M. D. Strauss, R. J. Wood, Monolithic fabrication of millimeter-scale machines. *J. Micromech. Microeng.* **22**, 055027 (2012).
26. F. C. Holsinger, J. S. Magnuson, G. S. Weinstein, J. Y. K. Chan, H. M. Starmer, R. K. Y. Tsang, E. W. Y. Wong, C. H. Rassekh, N. Bedi, S. S. Y. Hong, R. Orosco, B. W. O'Malley Jr., E. J. Moore, A next-generation single-port robotic surgical system for transoral robotic surgery: Results from prospective nonrandomized clinical trials. *JAMA Otolaryngol. Head Neck Surg.* **145**, 1027–1034 (2019).
27. K. Hwang, Y.-H. Seo, K.-H. Jeong, Microscanners for optical endomicroscopic applications. *Micro Nano Syst. Lett.* **5**, 1–11 (2017).
28. N. T. Jafferis, M. J. Smith, R. J. Wood, Design and manufacturing rules for maximizing the performance of polycrystalline piezoelectric bending actuators. *Smart Mater. Struct.* **24**, 065023 (2015).
29. N. T. Jafferis, E. F. Helbling, M. Karpelson, R. J. Wood, Untethered flight of an insect-sized flapping-wing microscale aerial vehicle. *Nature* **570**, 491–495 (2019).
30. J. M. Vassantachart, M. Lightfoot, A. Yeo, J. Maldonado, R. Li, M. Alsyouf, J. Martin, M. Lee, G. Olgin, D. D. Baldwin, Laser fiber cleaving techniques: Effects on tip morphology and power output. *J. Endourol.* **29**, 84–89 (2015).
31. R. Kiesslich, J. Burg, M. Vieth, J. Gnaendiger, M. Enders, P. Delaney, A. Polglase, W. McLaren, D. Janell, S. Thomas, B. Nafe, P. R. Galle, M. F. Neurath, Confocal laser endoscopy for diagnosing intraepithelial neoplasias and colorectal cancer in vivo. *Gastroenterology* **127**, 706–713 (2004).
32. P. R. Rizun, G. R. Sutherland, Surgical laser augmented with haptic feedback and visible trajectory, in *IEEE Conference on Virtual Reality* (IEEE, 2005), pp. 241–244.
33. L. Fichera, C. Pacchierotti, E. Olivieri, D. Prattichizzo, L. S. Mattos, Kinesthetic and vibrotactile haptic feedback improves the performance of laser microsurgery, in *IEEE Haptics Symposium* (IEEE, 2016), pp. 59–64.
34. E. Olivieri, G. Barresi, D. G. Caldwell, L. S. Mattos, Haptic feedback for control and active constraints in contactless laser surgery: Concept, implementation, and evaluation. *IEEE Trans. Haptics* **11**, 241–254 (2017).
35. S. Z. Mansour, R. J. Seethaler, Y. R. Teo, Y. K. Yong, A. J. Fleming, Piezoelectric bimorph actuator with integrated strain sensing electrodes. *IEEE Sens. J.* **18**, 5812–5817 (2018).
36. K. Jayaram, N. T. Jafferis, N. Doshi, B. Goldberg, R. J. Wood, Concomitant sensing and actuation for piezoelectric microrobots. *Smart Mater. Struct.* **27**, 065028 (2018).
37. J. Puig-Suari, C. Turner, W. Ahlgren, Development of the standard CubeSat deployer and a CubeSat class PicoSatellite, in *IEEE Aerospace Conference Proceedings* (catalog no. 01TH8542) (IEEE, 2001), vol. 1, pp. 347–353.
38. T. Mizuno, T. Kase, T. Shiina, M. Mita, N. Namiki, H. Senshu, R. Yamada, H. Noda, H. Kunimori, N. Hirata, F. Terui, Y. Mimasu, Development of the laser altimeter (LIDAR) for Hayabusa2. *Space Sci. Rev.* **208**, 33–47 (2017).
39. D. Grassani, E. Tagkoudi, H. Guo, C. Herkommer, F. Yang, T. J. Kippenberg, C.-S. Brès, Mid infrared gas spectroscopy using efficient fiber laser driven photonic chip-based supercontinuum. *Nat. Commun.* **10**, 1553 (2019).
40. H.-G. Kim, J.-N. Kim, T.-W. Na, K.-C. Park, I.-K. Oh, Motion control of piezoelectric tripod platform via feedforward hysteresis compensation. *Adv. Mater. Technol.* **3**, 1800298 (2018).

Acknowledgments: We thank all members of the Harvard Microrobotics Laboratory for advice and assistance, especially N. T. Jafferis for guidance on microrobotic transmission design and S. Bothner for contributions to the prior work out of which this research emerged. **Funding:** The authors acknowledge funding from the National Science Foundation (award #CMMI-1830291) and the Wyss Institute for Biologically Inspired Engineering. Any opinions, findings, and conclusions or recommendations expressed in this material are those of the authors and do not necessarily reflect the views of the National Science Foundation.

Author contributions: P.A.Y., R.P., D.K., and R.J.W. initiated and conceptualized the project. P.A.Y. conducted the design, fabrication, and experiments, and R.P. assisted with the colonoscope demonstration. P.A.Y. wrote the original manuscript, and R.P., D.K., and R.J.W. reviewed and edited the final manuscript. **Competing interests:** P.A.Y. and R.J.W. are inventors on patent application (PCT/US20/57684) submitted by Harvard University that covers the microrobotic laser steering technology described herein. The other authors declare that they have no competing interests. **Data and materials availability:** All data needed to evaluate the conclusions are included in the paper or the Supplementary Materials. Please contact P.A.Y. for additional materials and data requests.

Submitted 29 June 2020
Accepted 25 November 2020
Published 13 January 2021
10.1126/scirobotics.abd5476

Citation: P. A. York, R. Peña, D. Kent, R. J. Wood, Microrobotic laser steering for minimally invasive surgery. *Sci. Robot.* **6**, eabd5476 (2021).

Science Robotics

Microrobotic laser steering for minimally invasive surgery

Peter A. York, Rut Peña, Daniel Kent, and Robert J. Wood

Sci. Robot. **6** (50), eabd5476. DOI: 10.1126/scirobotics.abd5476

Science Robotics (ISSN 2470-9476) is published by the American Association for the Advancement of Science. 1200 New York Avenue NW, Washington, DC 20005. The title *Science Robotics* is a registered trademark of AAAS.